Optimization-based conformal path planning for *in situ* bioprinting in complex skin defect repair

Wenxiang Zhao[1,2], Chuxiong Hu[1,2 *], Yunan Wang[1,2], Shize Lin[1,2], Ze Wang[1,2], Tao Xu[3]

1. Department of Mechanical Engineering, Tsinghua University, Beijing 100084, China.
2. Beijing Key Laboratory of Precision/Ultra-Precision Manufacture Equipment and Control, Tsinghua University, Beijing 100084, China.
3. Center for Bio-intelligent Manufacturing and Living Matter Bioprinting, Research Institute of Tsinghua University in Shenzhen, Tsinghua University, Shenzhen, 518057, China.

* **Correspondence should be addressed to C. Hu (cxhu@tsinghua.edu.cn)**

Abstract

The global demand for effective treatments of prevalent skin injuries has prompted the exploration into tissue engineering solutions. While 3D bioprinting has shown promise, challenges persist in achieving timely and compatible solutions for treating diverse skin injuries. In response, *in situ* bioprinting has emerged as a new avenue, reducing risks during implantation of printed scaffolds, and demonstrating superior therapeutic effects. However, maintaining printing fidelity in *in situ* bioprinting remains a critical challenge, particularly concerning model layering and path planning. This study proposes a novel optimization-based conformal path planning strategy for *in situ* bioprinting repair of complex skin injuries. The strategy employs constrained optimization to find optimal waypoints on the point cloud-approximated curved surface, ensuring the highest similarity between predesigned planar and surface-mapped 3D paths. Furthermore, this method demonstrates applicability to skin wound treatment, generating 3D equidistant zigzag curves along the surface tangent and enabling multi-layer conformal path planning for volumetric injuries. The proposed algorithm proves feasible and effective in murine back injury model and other complex models, showcasing its potential to guide *in situ* bioprinting and enhance fidelity for improved clinical outcomes.

Keywords:

In situ bioprinting, path planning, robot control, skin injuries repair.

1. Introduction

The skin, being the largest organ in the human body, serves as a protective barrier against external elements[1]. Globally, prevalent skin injuries, such as burns and chronic ulcers, pose a great demand for effective treatments[2, 3]. While tissue engineering, particularly 3D bioprinting technology, has demonstrated its efficacy and potential[4, 5], practical challenges arise due to diverse skin injury characteristics, including shapes, depths, and locations[6, 7]. Tissue-engineered skin constructed using conventional benchtop bioprinter struggles to achieve an ideal match with the defect sites, and may risk contamination or destruction during implantation[8]. In response, *in situ* bioprinting, wherein bioink is directly deposited inside the defect in a clinical setting to create living tissues, has emerged as a new avenue to address these challenges[9]. This on-site approach integrates the traditional two-step "print-implant" strategy, thereby reducing potential risks during implantation and decreasing donor waiting time for tissue maturation in conventional bioprinting. Moreover, it has demonstrated superior therapeutic effects in soft tissue repair through animal experimental validations[10-15].

In *in situ* bioprinting, a critical objective is maintaining the printing fidelity, which is closely related to model layering and path planning in the pre-printing stage[8]. Unlike conventional bioprinting which is based on planar layering and printing on a flat surface, the substrate of *in situ* bioprinting is the defect with complex topographical features. Proceeding with planar layering not only leads to interruptions in the printing path but also brings a stair-step effect, inducing nonnegligible fabrication errors[16-18]. More importantly, this simplified layering pattern is not conductive to constructing tissue scaffolds that can directionally interface with native tissues, let alone slicing for different tissues separately in cases of composite tissue injuries, as indicated by Wang et al[19]. Therefore, the conformal layering method, where each layer bears similar profile to the topography of the skin defect, holds significant implications for *in situ* bioprinting.

Currently, research on conformal slicing in *in situ* bioprinting is limited, which has prompted us to focus on layering studies in multi-axis 3D printing. For instance, Mitropoulou et al., inspired by key-framing technique in animation, generates non-planar layers through smooth interpolation based on predefined curves and shape constraints of the designed structure[20]. This approach has shown effectiveness in thin-shell and bifurcating structures[21]. To improve slicing efficiency, Fortunato

extracts the outer surface of structures as the starting and ending layers, while adopting traditional planar slicing schemes for the intermediate unseen parts[22]. This hybrid approach ensures shape fidelity while reducing slicing complexity. Yigit and Lazoglu directly integrate slicing and path planning, proposing the spiral slicing method to eliminate interlayer seam defects[23, 24]. These studies in architecture and manufacturing[25] fields collectively highlight the necessity of conformal layering in improving shape fidelity, eliminating support structure, and enhancing efficiency.

In addition to model layering, conformality in path planning, which denotes the optimal compliance and similarity between the generated spatial path and the corresponding 3D surfaces[26], also contributes to printing fidelity. For determining printing path on 3D surfaces, current research typically relies on the surface's projection plane to plan 2D path, then extends it into 3D space[27-29]. Lian et al. designed a planar path based on two-dimensional information extracted from the scanned point cloud and subsequently utilized a lookup table to acquire the corresponding 3D waypoints[30]. Similarly, Zhou and colleagues used a comparable approach to generate spatial paths for printing demonstrations on living tissue surfaces[31]. Rodriguez-Padilla et al. proposed a method for generating curved printing paths by projecting discrete planar waypoints onto Stereolithography (STL) models and intersecting each waypoint with the triangles in the STL models to achieve better conformality[32]. These methods simply add an extra dimension to the 2D waypoints, neglecting the conformality of spatial paths with the surfaces. For instance, issues arising from the Euclidean distance between waypoints can result in varying internals of equidistant curves in the plane after mapped to three dimensions. Right angles in the plane, when projected, transform into sharp angles and abrupt turns. In a printing scenario, these problems might lead to defects such as overfilling or underfilling, and pose challenges to the positional and velocity control of the printing end-effector[28, 33]. Particularly for the skin wounds with unpredictable surfaces and complex borders, there remain obstacles in conducting in situ bioprinting to close the wounds with the desired precision. Some research in robotic trajectory planning[34, 35] adopts optimization methods to seek the optimal mapping of planar paths. These methods involve surface parameterization steps, thus present limited applicability. However, this optimization-based approach provides us with inspiration.Herein, we propose a novel optimization-based conformal path planning strategy for *in situ* bioprinting repair of complex skin injuries. The heart of this strategy is to formulate an objective function and employ constrained optimization

to find the optimal waypoints on the point cloud-approximated curved surface, ensuring the highest similarity in shape and angle between the predesigned planar path and the surface-mapped 3D path. In the realm of skin wound treatment applications, this strategy can be directly applied to the wound's point cloud, enabling the instant generation of 3D equidistant zigzag curves along the surface tangent without the assistance of 2D paths. Further, multi-layer conformal path planning can be achieved in combination with the conformal layering method for complex volumetric injuries. This optimization-based method involves the abstract fitting of the region of interest (ROI) in the point cloud, which does not require mathematical expressions of the substrate surface, thus showing favorable adaptability to irregular surfaces such as skin defects. Finally, several different conformal paths are generated on various surfaces to demonstrate the universality of the proposed strategy. Meanwhile, multilayer conformal paths are designed for wound filling on a murine back injury model, and *in situ* bioprinting is performed with a developed multi-DoF bioprinter. All these studies served to validate the feasibility and effectiveness of the novel path planning algorithm for *in situ* bioprinting.

2. Methods

2.1 Conformal path planning method based on optimization problems

The core of the proposed path planning algorithm can be summarized as discretizing a predefined path and then mapping each scattered points onto the surface with the objective of maintaining shape and angle. This section will primarily introduce the principles and processes of conformal path generation based on optimization problems, including parameter definition and the construction of optimization functions for shape preservation and angle preservation. Additionally, planar paths and 3D models are established for method verification.

2.1.1 Parameter definition

Consider a surface $S(x, y, z) \subset \mathbb{R}^3$, a planar path $P(u, v) \subset \mathbb{R}^2$, and a mapping relationship $r_s: \mathbb{R}^2 \to \mathbb{R}^3$, where $P_0(u_0, v_0)$ is the initial point in the path P and v_0 denotes the start direction of P. To obtain the global mapping of P onto S, a stepwise search is conducted on P with a step size of *stp*, where the angle between each stepping points is defined as θ. For the initial point, θ is defined as the angle between vec_0 and the x-direction of the coordinate axis. When optimizing the spatial stepping points on the surface S, l and w represent the length and width of the ROI in the point cloud of S, respectively. These parameters can be clearly identified in Fig. 1.

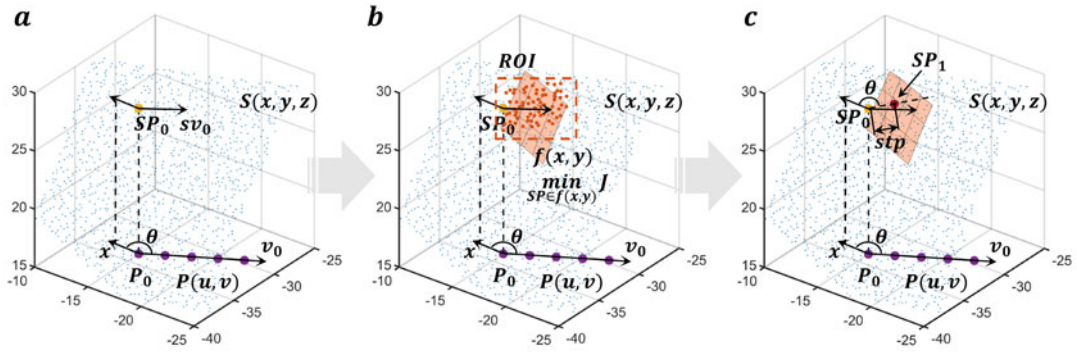

Figure 1. Illustrative flowchart of optimization-based conformal path generation. **a,** Given the planar path *P* and spatial point cloud *S*, the goal is to map *P* conformally onto *S*. P_0 and SP_0 represent the initial point, while v_0 and sv_0 represent the initial direction. **b,** Selecting the Region of Interest (ROI) on *S* and fitting a plane *f* based on the points within the ROI. **c,** Searching for the next point SP_1 on the fitted plane *f*, adhering to the constraints of shape and angle preservation.

2.1.2 Conformal Mapping with shape preservation

Based on $P_0(u_0, v_0)$, v_0, and *stp*, a portion of the point cloud can be filtered as the ROI, which is typically a narrow rectangular region starting from $P_0(u_0, v_0)$ and directed by v_0. Empirically, setting *l* as 1 times *stp* and *w* as 0.5 times *stp* enables accurate target point retrieval with a relatively small computational cost. Fitting the ROI with a quadratic surface, expressed as

$$\begin{bmatrix} x_1^2 & y_1^2 & x_1y_1 & x_1 & y_1 & 1 \\ \vdots & \vdots & \vdots & \vdots & \vdots & \vdots \\ x_m^2 & y_m^2 & x_my_m & x_m & y_m & 1 \end{bmatrix} \begin{bmatrix} a_{20} \\ a_{02} \\ a_{11} \\ a_{10} \\ a_{01} \\ a_{00} \end{bmatrix} = \begin{bmatrix} f(x_1, y_1) \\ \vdots \\ f(x_m, y_m) \end{bmatrix} \tag{2.1}$$

Where *a* represents the coefficients of the surface expression and *m* represents the number of points in the ROI. Commonly, the number of points *m* is sufficient to support surface fitting based on the least squares method, thus the equation of $f(x, y)$ can be acquired.

The essential requirement for shape preservation is to identify a mapped stepping point on surface *S* that minimizes the deviation between the geodesic path distance and the *stp*[34]. Hence, the optimization problem can be formulated as follows:

$$\begin{aligned} &\underset{SP}{\text{minimize}}\, J = \sum_{i=1}^{L} |\|SP_i - SP_{i-1}\| - stp| \\ &\text{subject to} SP \in f(x, y) \end{aligned} \tag{2.2}$$

Where L represents the number of segments into which the path P is divided by *stp*.

To solve the minimization problem, an interior-point optimization algorithm[36] is employed for constrained iteration, utilizing the fmincon function in MATLAB for implementation. Numerical optimization is sensitive to initial values, and choosing appropriate initial guess plays a crucial role in reducing the number of iterations and avoiding numerical divergence, when the convexity of the objective function J is not emphasized. Herein, the point in the ROI that is closest to the initial point in terms of distance to *stp* is selected as the initial estimate, which demonstrated rapid and accurate convergence in subsequent simulations and trials.

2.1.3 Conformal Mapping with shape preservation and angle preservation

In addition to good shape preservation, minimizing angular distortion is also desirable, as it helps maintain the structural and geometric similarity of the spatial path to the original path P in 2D. Similar to Equation 2.2, the optimization function with the objective of minimizing angular distortion can be described as follows.

$$\underset{SP}{\text{minimize}}\, J = \sum_{i=1}^{L-1} \left| \frac{(SP_{i-1} - SP_i) \cdot (SP_{i+1} - SP_i)}{\|SP_{i-1} - SP_i\| \|SP_{i+1} - SP_i\|} - \cos\theta \right| \quad \text{subject to } SP \in f(x, y) \tag{2.3}$$

However, on an irregular surface S, simultaneously optimizing for distance and angle as objectives is contradictory and poses challenges in terms of diversity and convergence during implementation. Hence, taking inspiration from cosine similarity and Euclidean distance in information retrieval[37], Equation 2.2 and 2.3 can be unified into a normalized model as shown below.

$$\underset{SP}{\text{minimize}}\, J = \frac{\sum_{i=1}^{L} \frac{|\|SP_i - SP_{i-1}\| - stp|}{stp}}{L} + \frac{\sum_{i=1}^{L-1} \left| \frac{(SP_{i-1} - SP_i) \cdot (SP_{i+1} - SP_i)}{\|SP_{i-1} - SP_i\| \|SP_{i+1} - SP_i\|} - \cos\theta \right|}{2 \times (L-1)} \quad \text{subject to } SP \in f(x, y) \tag{2.4}$$

The specific derivation can be found in the reference[38]. In this model, the parts representing distance and angle errors are separately normalized, ensuring their values within the range of (0,1). This normalization makes the optimization process of both parts equivalent in their impact on the objective function. The same interior-point optimization algorithm and initial estimation are used for this function, without introducing an extra increase in computational complexity. Equation 2.4 is used as the

objective function in subsequent research.

2.1.4 Examples of conformal path generation on 3D surfaces

To validate our fitting and optimization algorithms, we employed three surfaces as mapping substrates: a semi-ellipsoid with axes ratios of 11:10:9, a mathematical surface represented by $z = 0.5 \times \cos(x + \cos(y))$, and a folded origami protrusion structure in the shape of a hexagram. On each of these surfaces, various curves were mapped, including zigzag paths with varying intervals and orientations, square spirals, and simplified patterns of Chinese knots. For each mapping instance, the initial point on the surface is manually determined, and then, based on *stp*, the corresponding waypoints on the surface are decided using the optimization function 2.4. Within the optimization function *J*, the traversal step size of the 2D patterns is the only variable. Therefore, the part representing distance measurement J_d, and the part representing angle similarity J_a, as well as the computational time required for the optimization calculation, are recorded to determine a suitable *stp*. All the calculations were performed on a PC equipped with an Intel i7 and 8 GB RAM.

2.2 Conformal path generation strategy for wound repair.

Due to the strict conformal constraints of the proposed method, the coverage area will change when mapping the pre-defined planar path onto a curved surface. This is not conducive to the requirements for wound repair. As illustrated in Fig.2, if *in situ* bioprinting is carried out on the curved surface to fill the injury represented by red points, even though the 2D path planed in the projection plane is faithfully mapped onto the surface that avoids printing defects, the generated conformal path is unable to completely cover the injury. Therefore, this section will introduce improvements to the optimization-based path generation method in the wound repair scenario. This includes the process of directly generating conformal paths pointwisely on the surface without relying on a predefined planar path, as well as conformal layering and multi-layer paths generation method for filling volumetric wounds.

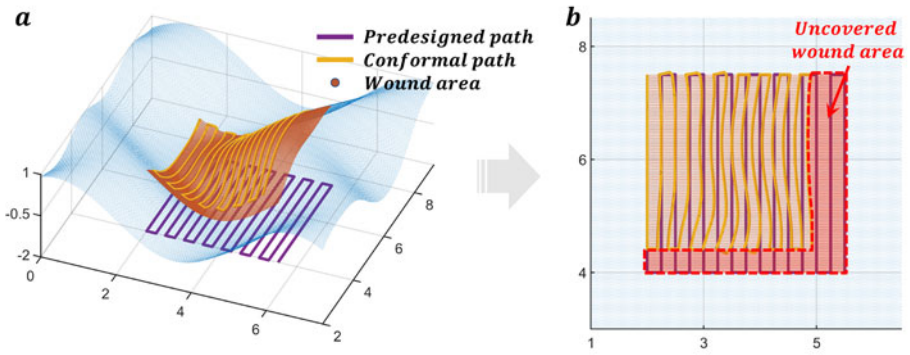

Figure 2. Limitations of the conformal projection method in wound coverage. a, Comparison of the pre-designed path and conformal path projected onto the wound. **b,** Top view showing partial uncovered wound area.

2.2.1 Single-layer path for wound coverage

The improvement of the optimization-based path planning method lies in directly generating conformal single-layer printing path on the surface without relying on pre-designed planar path. In this process, there is no discretization of pre-designed path; instead, the process iteratively searches for the optimal spatial point that strictly ensures maintaining the same spatial distance and linear constraints with the previous points. This search process also relies on the optimization objective function constructed in Section 2.1.

The zigzag pattern, as a common path in 3D printing, is characterized by its broad applicability, high continuity, and ability to meet the requirements of dense filling for tissue repair[39]. It is often used as a path pattern in research on bioprinting[40]. Therefore, this study also uses the zigzag pattern as an example to explore the direct generation of conformal repair path. Fig. 3 illustrates the schematic diagram of planning zigzag conformal paths directly on the surface based on optimization principles. Firstly, an initial point $P_{init.}$ and direction $V_{init.}$ are determined according to the wound area. Starting from $P_{init.}$, the next point is calculated stepwise on the surface with a spacing defined by *point_space*, also denoted as *stp*, until it exits the wound's region. The generated initial dot array is then scanned along the orthogonal direction $V_{orth.}$ with *line_space* as the parameter, until these waypoints traverse the entire wound area. *Line_space* describes the spacing between two adjacent paths, and its value is dependent on the printing process.

The connection of adjacent paths also follows the stepwise optimization strategy, utilizing $V_{orth.}$ and *point_space* as the stepping parameters while ensuring right-angle turns. It's noteworthy that a secondary check between the waypoints and the wound's

boundary is necessary to ensure alignment (as shown in Fig. 3b_3). If any points fall outside the wound area, their intersection with the boundary will be computed, or the nearest boundary point will be approximated to determine the waypoints. Additionally, considering the printed filament's width, inward indentation along the wound's edge is necessary, with the indentation parameter typically set to half the filament's width. Finally, the discrete waypoints are connected sequentially to generate a conformal printing path directly from the 3D point cloud of the surface.

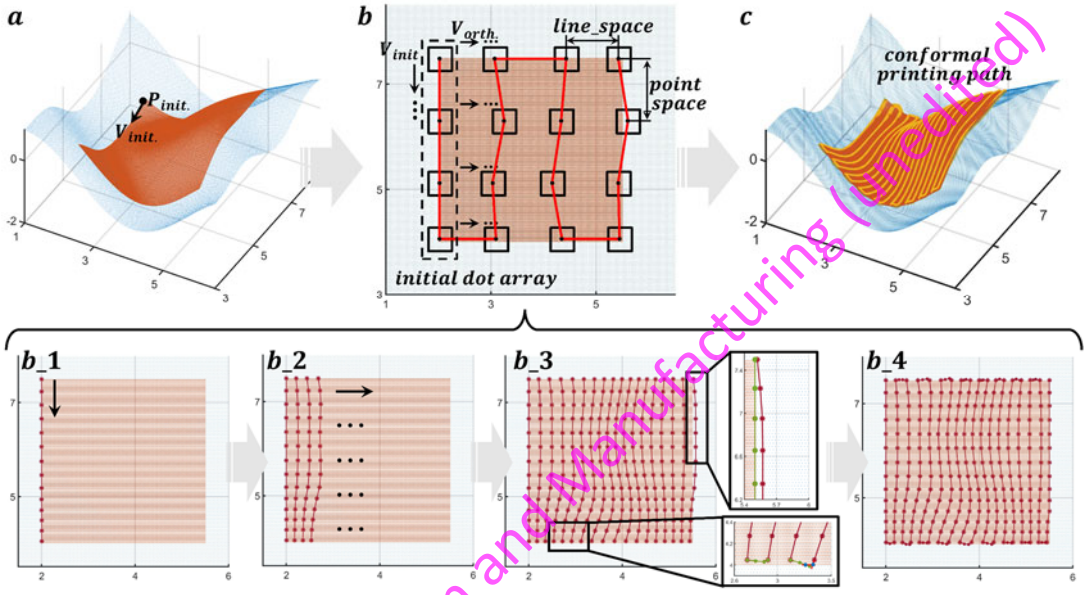

Figure 3. Flowchart of the direct conformal path generation based on the optimization method. a, Surfaces and wound regions (highlighted in red). **b,** Generation of the waypoints. **b_1,** Generation of the initial dot array based on V_{init} and *point_space*. **b_2,** Subsequent dot array generation based on V_{orth} and *line_space*. **b_3,** Checking edge dots based on the actual coverage area of the wound. **b_4,** Sequential connection of all waypoints. **c,** Conformal printing path in zigzag pattern covering the entire wound area.

2.2.2 Multi-layer path for wound filling

Layer-by-layer deposition is a fundamental process in 3D printing, while relying solely on acquired point clouds can only provide path information for a single layer, which falls short in addressing the volumetric filling and repair requirements of injuries. The point cloud hole-filling algorithm based on radial basis functions (RBF) is a well-established method for mending incomplete 3D models[41]. Briefly, it leverages boundary information from the hole of point cloud, computing the average distance, angle, and curvature of the neighboring points. By searching for points that conform to

the prescribed patterns of variation in these three criteria, the algorithm progressively fills the hold until complete restoration is achieved. Herein, RBF is an implicit surface that can be controlled by discrete points in a point cloud, enabling smooth interpolation of scattered spatial data. In the context of injury repair tasks in this study, the point cloud at the defect sites is removed, and an implicit surface is constructed using Gaussian-shaped basis functions to generate a point cloud that exhibits curvature variations similar to the healthy skin without injuries. The original point cloud is then subjected to Boolean operations with the interpolated points, resulting in an enveloping space that denotes the region requiring filling with bioprinting.

The initial layer of the conformal path is generated on the original point cloud of tissue injury with the method described in Section 2.2. Due to the certain thickness of the printed filament, the second layer path can be generated on the point cloud obtained by offsetting the initial layer path along the normal direction at each waypoint. Points exceeding the uninjured skin in the point cloud filtered out, obtaining the point sets for path planning. This approach ensures the similarity of the shape between each newly generated point cloud and the original wound, thus achieving conformal layering. The conormal path for the current layer is then planned through the same method. For obtaining point clouds of higher layers, the normal vectors captured from the scanning data in the initial layer cannot be reused. Hence, a Kd-tree is used to organize the point cloud structure, and the approximate local normal vector for each point is calculated based on it. The specific construction of kd-tree relies on the open-source library VLFeat[42]. It's noteworthy that in cases where the normal vectors of the wound are approximately parallel to the healthy skin, the newly generated point cloud by normal vector offset may be smaller than the healthy skin's coverage area, which can result in incomplete filling of the defect. In such situations, the overall principal component direction of the entire wound area can be obtained to offset the point cloud as a whole along the principal component direction, thus filling the incomplete area. Following this procedure, the conformal layering and conformal path planning steps are repeated until the volumetric injury is completely filled, as shown in Fig. 4. Finally, these conformal paths from each layer are connected in sequential order according to the nearest neighbor principle, achieving multilayer conformal path planning for volumetric injuries.

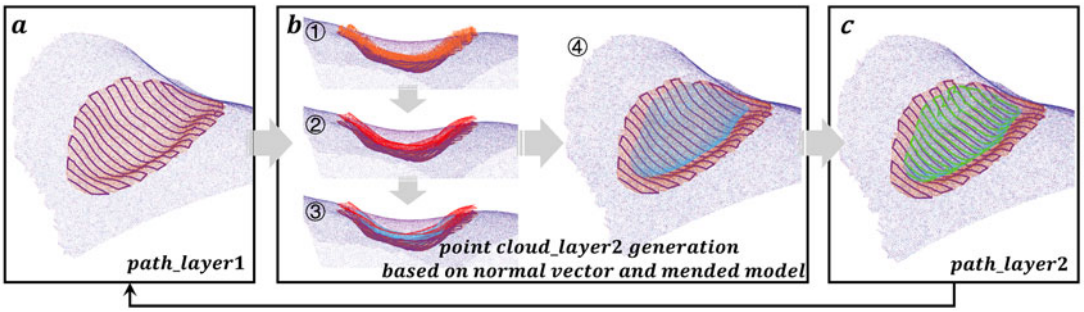

Figure 4. Flowchart of multilayer conformal path generation. a, Generation of path_layer1 on the original point cloud. **b,** Strategy for generating point cloud_layer2. **①,** Obtaining path's normal vector based on path_layer1 and the original point cloud. **②,** Generating point cloud_layer2 based on the normal vectors and layer thickness. **③,** Taking the intersection of point cloud_layer2 with the RBF-repaired point cloud. **④,** Obtaining the final point cloud_layer2 that to be repaired. **c,** Generation of path_layer2 on point cloud_layer2, and so forth.

2.3 Design and processing of point cloud models

This study involves four types of three-dimensional models: ellipsoidal surface, mathematical surface, folded protrusion surface, and a murine back wounds model. The first three models were designed in CAD software (Solidworks, Dassault Systemes), exported as STL files, and subsequently converted in to point cloud models using Geomagic Studio software (Morrisville, NC, USA). Point cloud redistribution was then performed to ensure uniform point cloud density across the models. In addition, these models were physically constructed via photosensitive 3D printing for practical *in situ* printing validation. The murine dorsal wound was established in our previous study [11], wherein we created four wounds of different sizes, locations, and depths on the murine back. A structured light 3D scanner (HSCAN-S, Thunk3D, China) was used to capture the wound model of complex tissue skin tissue defects and obtain their 3D point cloud. Due to the small size of nude mice, it was not feasible to plan multi-layered paths on the scanned point cloud, thus further limiting the effectiveness of validating the proposed algorithm. Therefore, the scanned point cloud model was scaled up by 5 times to serve as the object to plan conformal paths for wound repair. Similarly, the upscaled model was encapsulated and 3D printed to create physical model for practical printing validation of the proposed path generation method.

2.4 Materials and hydrogel preparation

Methacrylate gelatin (GelMA) and lithium phenyl-2,4,6-trimethylbenzoylphosphinate (LAP) were purchased from EFL Inc. (Suzhou, China),

and prepared into precursor solutions according to the instructions. Briefly, a predetermined amount of lyophilized GelMA was weighed and thoroughly dissolved with magnetic stirring in phosphatic buffer solutions (PBS) with 0.5% LAP at 40 ℃, resulting in a final GelMA concentration of 10%. Edible dye was added to enhance its visibility, and the prepared solution was stored at 4 ℃ until further use.

2.5 Experimental setup and printing process

The printing device utilized in this study is a seven-axis bioprinting robot developed previously[14, 43]. Its serial structure and redundant configuration demonstrate advantages such as favorable manipulability in *in situ* bioprinting, and it possesses a trajectory tracking accuracy of approximately 0.17 mm[14]. The difference lies in the simplification of the printing end-effector. Specifically, applying Ruhr needles shortens the actuator's length and diminishes the distance that the bioink travels during the injection. This adjustment aims to alleviate the influence of shear effects on the hydrogel's condition during the printing process[44], allowing for a better illustration and comparison regarding the impact of path planning on the printing outcomes. The printed hydrogel structure undergoes temporary deposition through a thermosensitive process. Upon the completion of printing, secondary curing is performed by irradiation with a 405nm wavelength LED surface light source (light irradiance: 100 mW/cm^2, exposure time: 20 seconds). The final end-effector was installed at the flange of the seven-axis robot. By employing tool center point (TCP) calibration, the homogeneous transformation matrix of the end-effector was obtained and incorporated into the proposed robot kinematic control algorithm[14]. The designed printing targets were created and aligned with the coordinate system of the bioprinting robot manually for subsequent printing experiment.

During the printing process, ensuring uniform filament deposition requires maintaining a consistent TCP velocity along the surface. However, the mapping between TCP velocity and joint velocity is highly nonlinear[45]. The methodology for planning the robot's printing trajectory was guided by this study.[46] In simple terms, the generated path was divided into uniformly spaced discrete points, allowing the TCP to move at a consistent speed between adjacent points. Furthermore, to ensure continuous changes in the TCP orientation, a tolerance θt for printing angle is introduced. The introduced tolerance, θt, ensures that the printing nozzle remains within a conical region defined around the surface normal vector. By selecting appropriate nozzle orientations within this region, the priority is given to ensuring uniform and

continuous linear speed along the entire path.

2.6 Printing experiment analysis of path planning algorithm

The evaluation of the path planning algorithm is conducted through actual printing experiments and image analysis. First, the *line_space* parameter is determined based on the printing filament width, ensuring that the material printed along the specified path can precisely cover the area of the reference trajectory. Traditional projection-based path planning approach might lead to overfilling or underfilling defects in curved surface printing. Therefore, printing paths are separately designed using both the traditional method and the optimization-based approach proposed in this study, follow by actual 3D printing experiments. After printing, top-view photographs of the printed structures are captured with a camera and subsequently analyzed using image analysis software (ImageJ, NIH).

The quantitative evaluation of the printing effectiveness relies primarily on three parameters: *Sd*, which refers to the area covered by the designed trajectory, representing the intended printing area. The area covered by extending the planned path along the line width is defined as *Se*, and the coverage area of the printed structure is defined as *Sp*. The fidelity of the in situ bioprinting process on this curved surface can be evaluated through the relationship between *Se* and *Sp*, indicating whether the printed structure matches with the theoretically designed one. Similarly, the effectiveness of the planned path in achieving complete coverage on the surface can be evaluated through the relationship between *Sd* and *Sp*. It assesses whether the printed structure exhibits overfilling or underfilling deficiencies and whether it can achieve high-precision coverage of the wound area.

2.7 Printing experiment analysis of wound repair path

For the printing experiment analysis of wound repair path performed on the dorsal wound model, the first step involves removing the wound area from the obtained point cloud model. Then, utilizing the RBF hole-filling algorithm based on the curvature of healthy skin areas, the missing skin can be filled to generate a simulated healthy dorsal skin model as the target. Subsequently, following the method described in Section 2.2.2, multi-layered printing paths are generated for different wounds to guide the 7-axis bioprinting robot for in situ bioprinting process. After physical he printing, the 3D scanner is employed again to capture the surface point cloud of the printed model. This model and RBF-filled model are imported into the Geomagic Studio software, and registered based on feature points. Upon completion of the registration process, the

built-in deviation calculation function is utilized to compute deviation heatmaps between the two models, assessing the accuracy of the bioprinting for wound repair.

3. Results and discussion

3.1 Selection and analysis of step size parameter

As described in Section 2.1, during the optimization process of the printing path, the search step size *stp* is one of the few parameters that can influence the alignment consistency between the path and the surface. As shown in Fig. 5a, when the flat predefined path is mapped onto the surface, taking three intermediate points as examples, the distance between these points on the flat path is *stp*, and the angle between them is 180°. However, when mapped onto the surface, the constraint objective is to ensure that the distance between adjacent points along the surface is *stp*. The Euclidean distance between them, calculated by $\|SP_i - SP_{i-1}\|$ (i.e. stp_r), is inevitably not equal to *stp*, leading to distance errors (Fig. 5b). Meanwhile, the three mapped points are all on the curved surface. The convexity of the surface shatters the goal of faithfully projecting angles, meaning that ensuring 180° angles cannot be guaranteed. This issue is ineluctable and can only be mitigated by selecting an appropriate *stp* to minimize distance and angle errors. Taking Fig. 5c as an example, when *stp* decreases from 3 to 1, both distance error (J_d) and angle error (J_α) significantly decrease from 0.011 to 0.001.

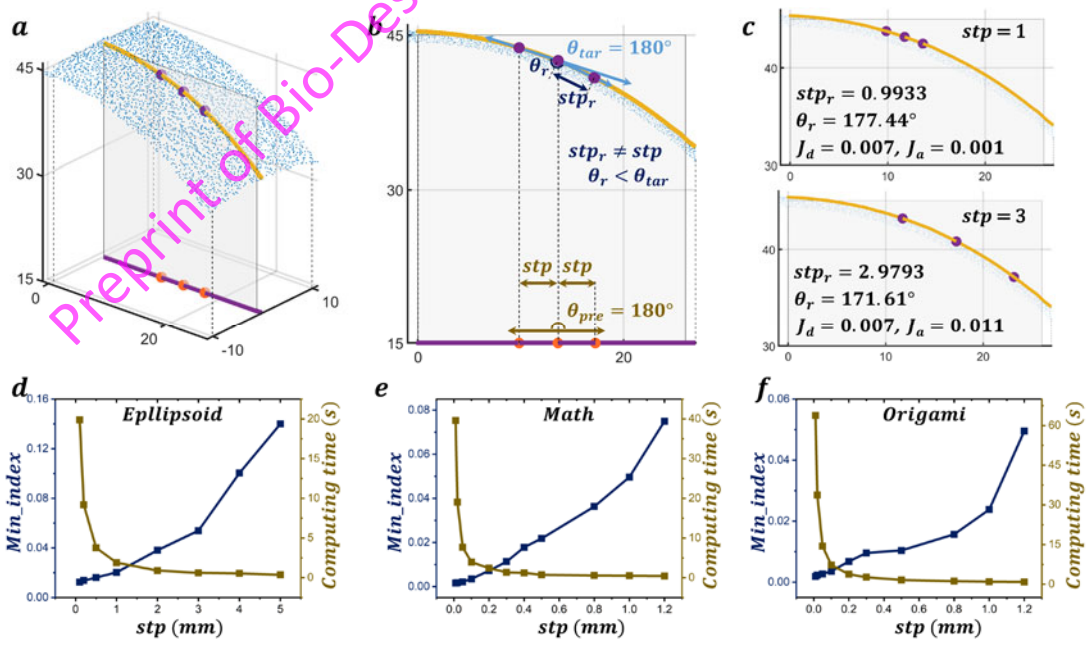

Figure 5. Effects of the step size on projection results. a, Overall schematic. **b,**

Projecting planar waypoints onto a surface changes both stp_r and θ_{tar} due to the surface curvature. **c,** The stp_r and θ_{tar} and overall deviation J obtained from different *stp* values. **d-f,** Trend plots of overall deviation J and computation time corresponding to different *stp* values on ellipsoid **(d)**, math surface **(e)** and origami surface **(f)**.

The decrease in *stp* leads to an increase in computation complexity and, consequently, an increase in computation time. To explore the trends in error and computational complexity caused by varying *stp*, we conducted path mapping and statistical analysis on ellipsoidal, mathematical, and origami surfaces using different *stp* parameters, as shown in Fig. 5d-f. The consistent conclusion is that as *stp* decreases, the required computational complexity exponentially rises, while the reduction in error becomes limited with further reduction of *stp*, making the option not worthwhile. The errors and computation time were plotted together, and the intersection point of the two curves was initially chosen as the optimal *stp* value, which simultaneously achieved lower mapping error and computational complexity. The optimal *stp* values for the three surfaces and their respective point cloud densities were analyzed in Table 1, revealing the following patterns.

$$\text{Density} * l\_opt * w\_opt \approx 20 \tag{3.1}$$

Where l and w represent the length and width of the ROI, and l_opt equals to optimal *stp*, w_opt equals to half of the optimal *stp*, as described in Section 2.1.2.

Table 1. Summary of point cloud density and optimal stp.

Surface type	Density (cm^{-2})	Optimal *stp* (mm)	J	Computation time (s)
Ellipsoid	1.5×10^4	1.30	0.0249	2.36
Math	1.1×10^5	0.210	0.00942	2.45
Origami	1.8×10^5	0.110	0.00364	6.25

Empirical equation 3.1 indicates that for a surface with given density, the *stp* value obtained through it strikes a balance between computation speed and error reduction requirements, making it a favorable choice for the step size in path generation. This provides valuable guidance for selecting step lengths in optimization-based conformal path generation on unknown surfaces. The theoretical basis of Equation 3.1 can be

explored as follows: it represents the ideal number of scattered points within the ROI. As described in Section 2.1.2, both the length and width of the ROI are denoted by *stp*. When considering dimensions, the multiplication of the length and width cancels out the denominator associated with the density dimension, leaving the number of scattered points as the unit. There are approximately 20 points in each ROI, which is a suitable quantity for fitting a quadratic surface. This adequacy has been supported by other studies[47-49], reinforcing the applicability of the proposed empirical formula theoretically.

3.2 Comparison between conformal path and direct-project path

The pursuit of conformality in projecting planar paths onto curved surfaces holds practical significance. For instance, in path planning based on zigzag patterns during 3D printing, the consistent spacing of the curves aids in achieving uniform filament deposition, thereby preventing printing defects such as overlaps or gaps. As shown in Fig. 6a, when mapping the zigzag path onto the elliptical surface in different approaches, the curvature increase underneath the ellipsoid causes the spacing *Dd* of paths generated with the direct projection method to widen, leading to a loss of its equidistant characteristics. Integrating the constraint of preserving angle into account, the right-angle turns in the zigzag path has been spatially optimized according to the surface characteristics, as illustrated in Fig. 6b. The necessity of preserving angles is more apparent in the manufacturing ad application of conformal antennas. Such as constructing conformal antennas on surface using the 3D direct-write approach, even subtle changes in morphology can lead to alterations in electrical properties[50, 51].

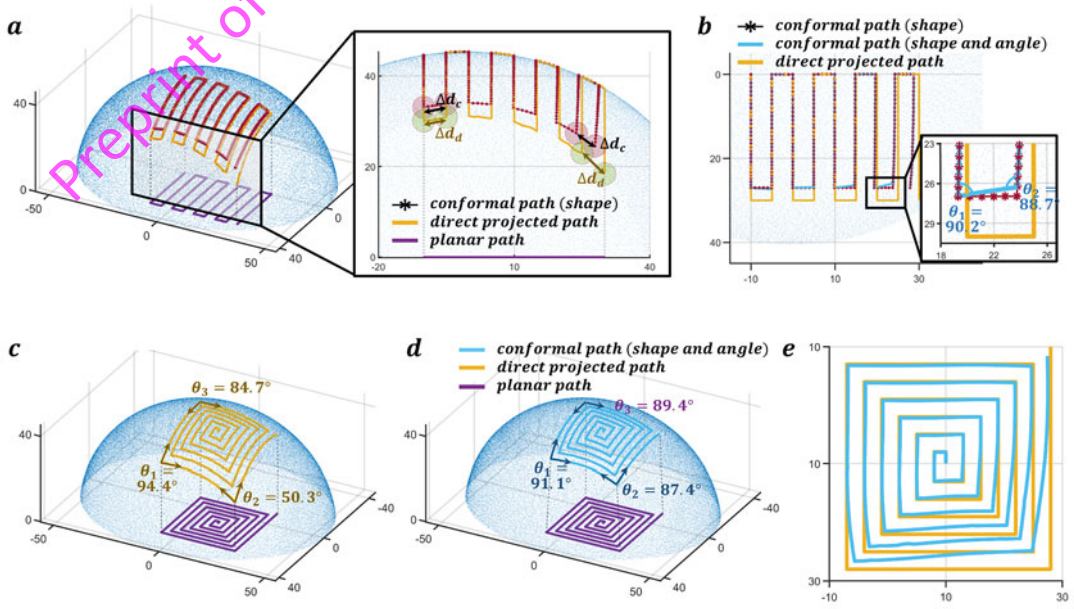

Figure 6. Comparison between conformal path and direct-project path. a, Conformal path with shape preservation for maintaining equidistant curves. **b,** Conformal path with shape and angle preservation. **c,** Distortion effect of direct-project path on right angles**. d,** Conformal path preserving right angles. **e,** Top-view comparison of conformal path and direct-project path.

In Fig. 6c, square spiral curves with multiple right-angle turns, when directly projected onto the ellipsoidal surface, experience distortion in certain corners, with the most notable instance changing from 90° to 50.3°. However, spatial path generated under conformal constraints can maintain each turn angle near 90°, with a maximum deviation controlled within 0.05 rads (Fig. 6d). The top-view comparison of these two paths is illustrated in Fig. 6e. The practical value of this angle preservation has also been confirmed by studies conducted by Adams and colleagues, demonstrating its significance in spherical antennas printing-based fabrication[51].

3.3 Conformal mapping illustrations from plane to surface

To explore the applicability of the proposed conformal path planning method for different types of curves and surfaces, further testing was conducted based on the presets outlined in Section 2.1.4. Specifically, three pre-planned complex planar paths were conformally mapped onto three types of point cloud surfaces. During the stepwise searching processing for conformal points, the equation 3.1 was employed to select suitable *stp* values for each surface. Under the optimization-based conformal path generation strategy, all spatial paths demonstrate high conformality, as indicated by green lines (Fig. 7). The corresponding relative errors, all within the order of 10^{-2}, are listed below the images. The maximum angular deviation in all demonstrations does not exceed 0.1 rads, and the time required for generating all conformal path is within 6 seconds. Correspondingly, the surface paths generated through direct projection approach are also presented in Fig. 7 with red lines. A comparison between the top views of the zigzag path and the square spiral path reveals the faithful reproduction of curve equidistance and right-angle elements achieved by our proposed conformal strategy. When applying the direction projection approach, distortions in the patterns may occur, potentially leading to defects during the printing process. This will be further validated in subsequent practical printing experiments.

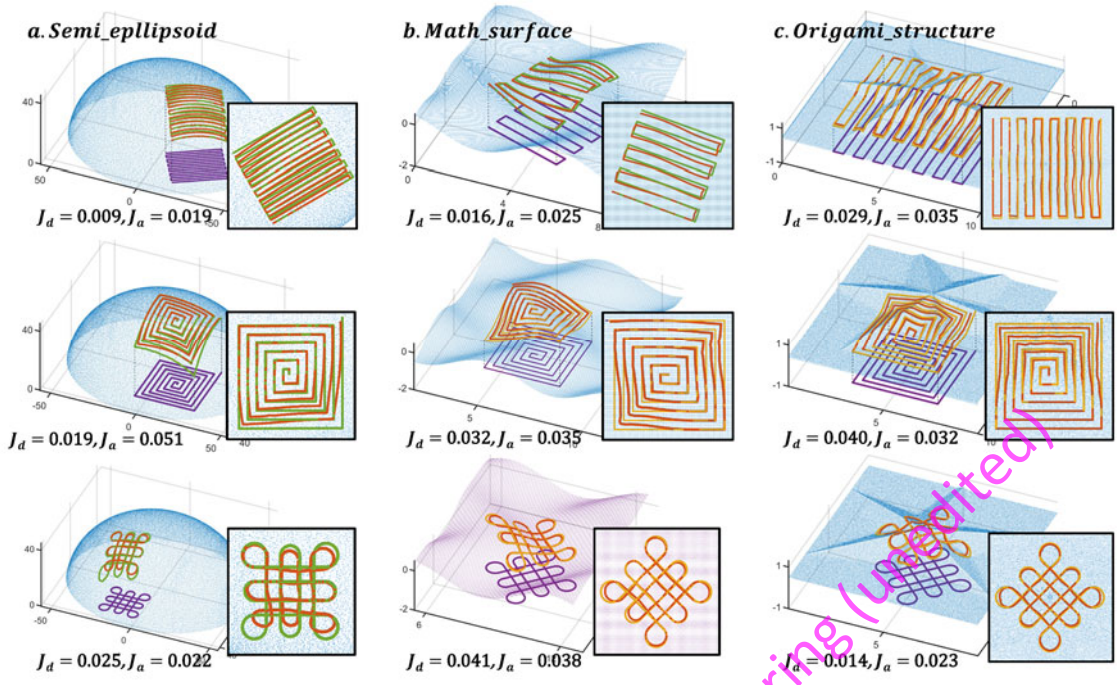

Figure 7. Conformal mapping illustrations from plane to surface. a, Semi ellipsoidal surface. **b,** Mathematical surface. **c,** Origami structure. (Deviations are listed below each image, with J_d representing distance deviation and J_α representing angle deviation.)

3.4 Bioprinting validation and analysis on geometric models

Through the optimization of step size parameter in Section 3.1, the superiority of conformal path over direct-project path in Section 3.2, and the validation of applicability across various curves and surfaces in Section 3.3, the comprehensive advantages of the proposed conformal path planning method have been observed. Next, it is necessary to evaluate the effectiveness of the planned paths in guiding the in situ bioprinting as well as the advantages of conformal paths in reducing printing defects based on the practical printing results.

Three representative patterns in Section 3.3 were selected for practical bioprinting experiments to validate the guiding effectiveness of the conformal paths. Fig. 8a_1-c_1 shows the pre-designed conformal paths on the point cloud surfaces, while Fig. 8a_2-c_2 depict the actual printing results. Preliminary assessment from the photos suggests that the proposed *in situ* bioprinting strategy, encompassing materials, equipment, and path generation method, can construct the desired patterns on complex surfaces with high fidelity, closely aligning with the predetermined paths. The quantitative evaluation, as described in Section 2.6, involves extending the top view of the predetermined paths

by the width of printing filament, i.e., 0.18mm. The resulting area *Se* and actual printed area *Sp* are depicted in green and blue separately. In the three presented examples, the pixel areas occupied by *Se* and *Sp* are essentially the same. Three independent testing for each cases reveals an average deviation of *Sp*/*Se*, approximately 96.9% ± 1.6%, 97.2% ± 0.8%, and 95.5% ± 2.1%. Specific variations occur depending on the curvature of the surface and the characteristics of the predefined path, but overall demonstrating high fidelities.

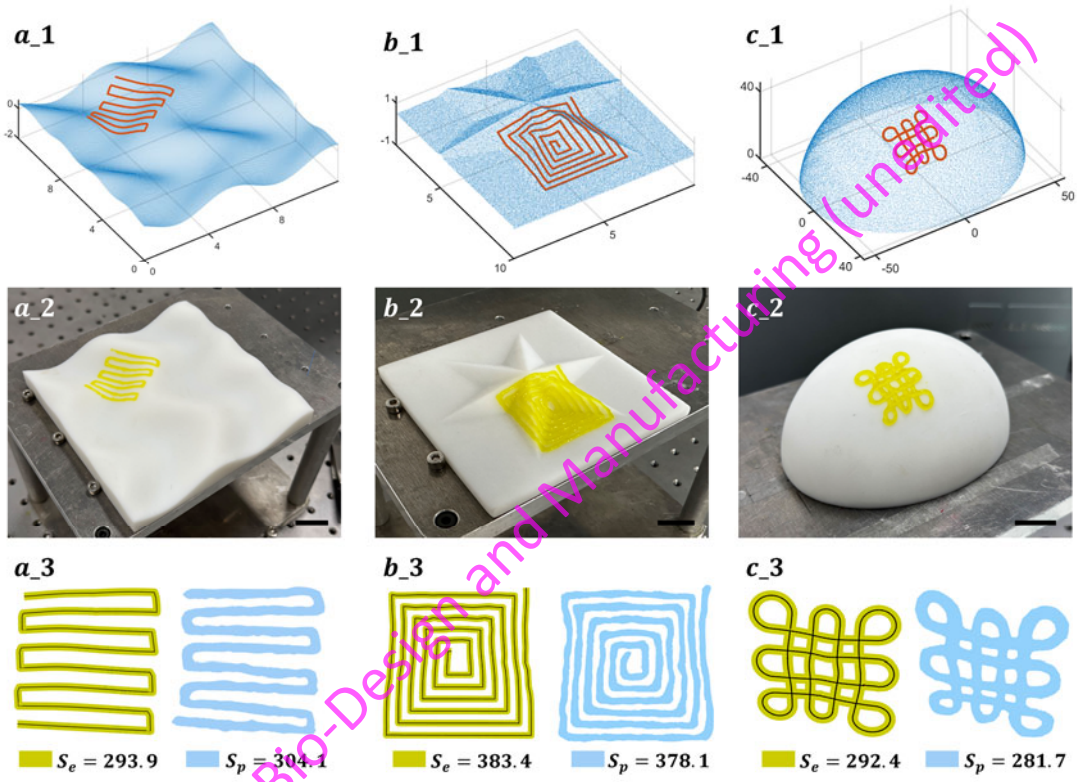

Figure 8. Bioprinting validation on geometric models. a, Zigzag path on the mathematical surface**: a_1,** Model in MATLAB. **a_2,** Actual printing image. **a_3,** Comparison of theoretical coverage area and actual coverage area. **b,** Square spiral path on the origami structure. **c,** Chinese knot pattern on the ellipsoidal surface, where 1-3 represent the same images as above. (Scale bar for subplot 2: 2 cm). ***Se***: the area covered by extending the planned path along the line width. ***Sp***: the coverage area of the practical printed structure.

Subsequently, a comparison is performed between conformal paths and paths generated through the traditional direct projection method using a dense filling approach (Fig. 9). Zigzag patterns are employed for path planning on these surfaces, where the line spacing is determined by the filament diameter, i.e., 0.18mm. In each case, the left side depicts the results of conformal path, while the right side illustrates

that of direct-project path. The practical coverage areas are still calculated and juxtaposed with the designated coverage area (outlined by dashed lines). The results indicate that, in the printing process with direct-project path, defects involving insufficient filling commonly occur in regions with significant curvature changes, such as the troughs of mathematical surfaces or the corners of folded structures. The ratios between *Sp* and *Se* indicate that in the dense arrangement of conformal paths, the printing replicability of these paths remains around 98.1% ± 0.7%, once again demonstrating the stability of the *in situ* bioprinting process. In contrast, direct-project paths exhibit a lower coverage rate of the preset area, approximately 93.6% ± 2.1%, due to the presence of gap defects. The area of these gaps, denoted as *Sh*, is also calculated, and annotated in the corresponding figures, occupying about 3.1% ± 1.2% of the preset area. The proportion varies with surface types and their local curvature. These practical printing experiments collectively affirm the necessity of constructing conformal paths in *in situ* bioprinting conducted on curved surfaces.

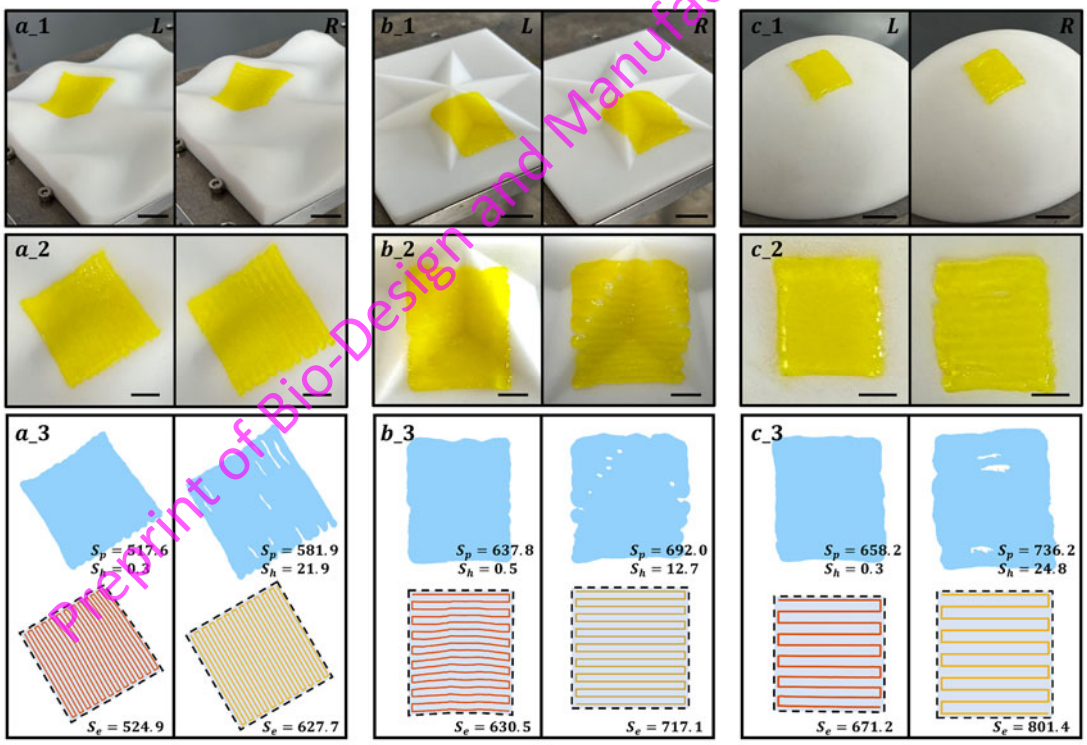

Figure 9. Bioprinting validation of dense pattern on geometric models. a, Zigzag path on the mathematical surface. **a_1,** Actual printing image. **a_2,** Top view of the actual printing image. **a_3,** Comparison of actual coverage area and theoretical coverage area. **b,** Zigzag path on the origami structure. **c,** Zigzag path on the ellipsoidal surface, where 1-3 represent the same images as above. (Scale bar for subplot 1: 2 cm, and for subplot 2: 1cm). **L:** Left, represents the conformal path

method. **R:** Right, represents the direct projection method. ***Se***: the area covered by extending the planned path along the line width. ***Sp***: the coverage area of the practical printed structure. ***Sh***: the area of underfilling gaps in the printed structure.

3.5 Bioprinting validation and analysis on skin wounds model

Section 3.4 has demonstrated the effectiveness of the proposed method in guiding the high fidelity *in situ* printing on 3D surfaces. The focus will now shift towards the practical application scenario of skin wound repair. This involves directly generating multi-layer conformal paths within complex skin wounds to guide the complete repair through *in situ* bioprinting. For generating conformal paths on irregular and complex point clouds, as illustrated in Fig. 10, the approach is similar to that described in Fig. 3. It is essential to note that path planning generally follows the principal component direction of the wound, aiding in achieving better coverage of the wound with a dense pattern[19, 52]. Once the principal direction is determined (Fig. 10c_1), a point-by-point search is conducted along its orthogonal direction for the widest part of the wound, constructing the initial dot array. Following this, the search extends along the principal direction on both sides, rigorously adhering to the constraint of maintaining equidistant curves, until the point cloud is comprehensively covered with any omissions (Fig. 10c_2). Finally, the waypoints located inside the point cloud are preserved and connected sequentially, forming a zigzag conformal path that covers the irregular wound (Fig. 10c_3).

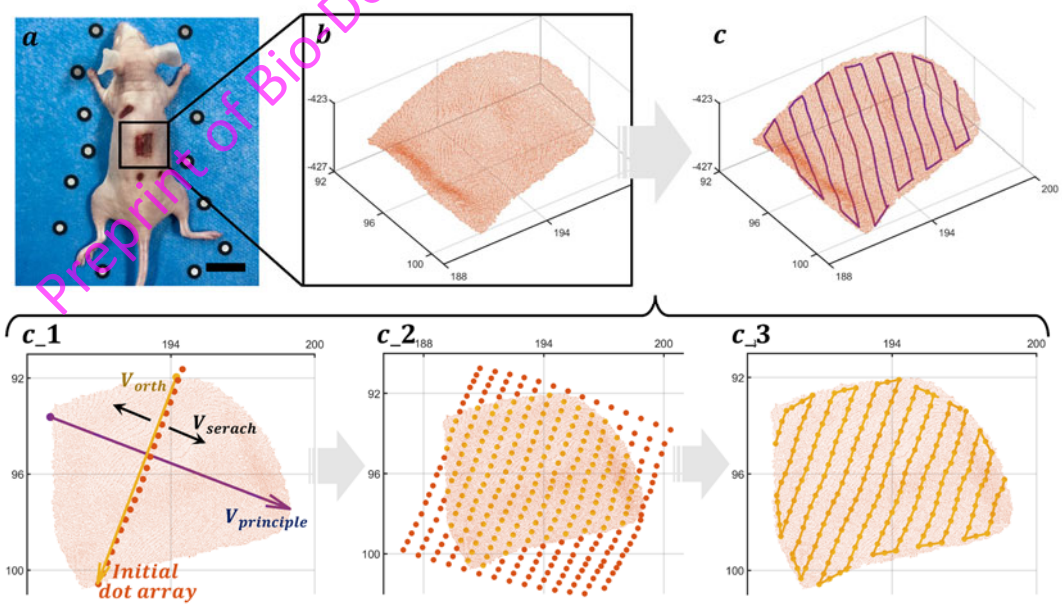

Figure 10. Conformal path generation strategy for actual wound coverage. a, Image of a mouse with created back wounds (Scale bar: 2 cm). **b,** 3D scanned point

cloud of one of the wounds. **c,** Conformal path generation for complete wound coverage. **c_1,** Determination of search direction and initial dot array based on the principal component direction and the widest part. **c_2,** Extension of the initial dot array along the search direction until complete coverage of the entire wound. **c_3,** Exclusion of waypoints outside the wound, followed by sequential connection of all these points.

As described in Section 2.2, in the generation of repair paths covering wounds using the zigzag pattern, the adjustable parameters describing the zigzag path include *point_space*, *line_space*, and *indentation*., Due to the point-to-point motion pattern of the bioprinting robot, an excessively large *point_space* can result in mismatches between the zigzag path and the complex surfaces. The conformal paths with different parameters on the point cloud of the skin wound again demonstrate the detrimental contribution of inappropriate *point_space* to mismatches (Fig. 11a-c). In such a context, the *point_space* parameter and the step size *stp* optimized in Section 3.1 have consistent effects, aiming to achieve the highest similarity between the generated path and the target repair surface. Therefore, for a known density of determined point clouds, setting *point_space* equal to *stp* will result in optimal high-fidelity in situ bioprinting outcomes. *Line_space* determines the search distance on both sides of the initial dot array. Achieving a dense arrangement of printed threads is often necessary when filling and treating skin wounds[27, 52], therefore, it is essential to figure out the *line_space* parameter through preliminary experiments before path planning. Fig.11d-e showcase repair paths with different *line_space* values. When determining *line_space* and expanding the initial dot array on the surface based on this parameter, it is generally advisable to avoid selecting *line_space* as the search step. Normally, *line_space* parameter is typically larger than *point_space* (stp), leading to an increase in mapping error due to the larger search step. Therefore, during the expansion process of the initial dot array, *line_space* is divided into multiple segments based on *stp*. The search for target points at a distance of *line_space* from the starting point is still conducted with *stp* as the step size, ensuring equidistant characteristics during the expansion process. Indentation is also a vital parameter. To ensure a precise alignment of the printed structure with the boundaries of the wound, it is required to inwardly shrink the originally planned path by a certain width. Taking the 0.18 mm as an example, the comparison between the shrunk path and the original path is illustrated in Fig. 11f.

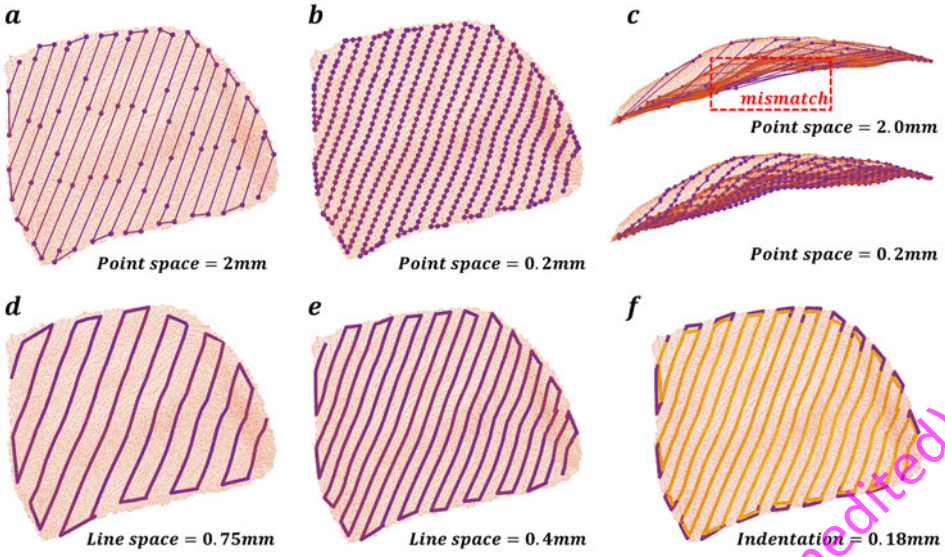

Figure 11. Conformal path on wound surfaces with different parameters. a, *Point_space* set to 2. **b,** *Point_space* set to 0.2. **c,** Side view of the path and surface, showing mismatches at regions of high curvature. **d,** *Line_space* set to 0.75. **e,** *Line_space* set to 0.4. **f,** Indentation parameter set to 0.18.

For these created skin wounds, achieving complete wound coverage often necessitates multi-layer path planning. Based on the model processing method in Section 2.7 and the multi-layer path generation strategy outlined in Section 2.2.2, the area to be repaired is delineated by blue and deep red borders (Fig. 12b-d). The thickness of the printing filament (normally 1 mm) and the actual depth of the wound dictate the number of printing layers, continuing until the wound is completely filled. The final obtained wound repair paths are depicted in Figure 12.For instance, Wound 1 involves 5 layers of paths, while the smaller Wound 3 only requires one layer to be treated. Additionally, in the conformal paths, the normal vector at each waypoint aligns with the surface normal vector, constraining the pose of the bioprinting robot's end effector. This ensures that during the actual bioprinting process, the robot's nozzle adapts to changes in the local surface normal vector while moving along the path. In *in situ* bioprinting, the strategy of increasing the printing angle (angle between the printing nozzle and the surface tangent) can achieve more precise bioink deposition[53].

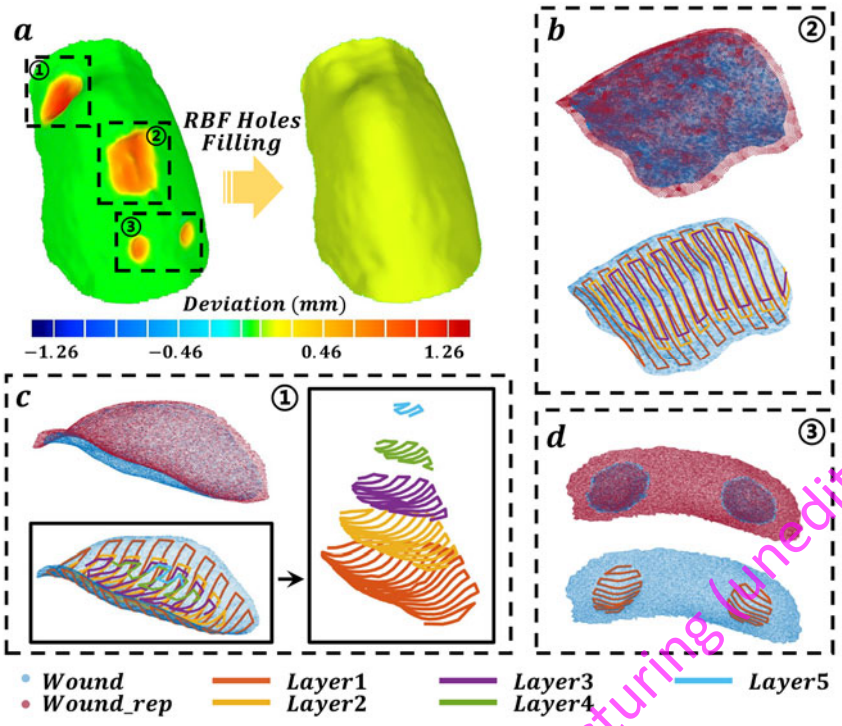

Figure 12. Multi-layer path planning on mouse back wound models. a, Using the RBF method to fill the scanned mouse back wound into a smooth model, simulating the undamaged skin state. **b,** The areas to be filled and the planned multi-layer paths for wound 2. **c,** The areas to be filled and the planned multi-layer paths for wound 1. **d,** The areas to be filled and the planned conformal paths for wound 3.

The real printing process is shown in Fig. 13. The left image depicts an overview of the setup, where the end effector of the seven-axis bioprinting robot is a self-developed tool capable of quantitatively extruding bioink. Fig. 13b present the process of repairing wounds 2 and 3, where the comparison between Fig. 13b_1 and Fig. 13b_2 reveals the deposition of multiple layers of hydrogel. Similarly, Fig. 13c illustrate the complete process of repairing wound 1, with each image corresponding to 1 layer (Fig. 13c_1), 2 layers (Fig. 13c_2), 3 layers (Fig. 13c_3), 4 layers (Fig. 13c_4) and 5 layers (Fig. 13c_5), finally achieving the complete filling of the wound. Observing the printing results, in wound 1 with an inclined orientation, despite the strict alignment of the nozzle with the wound surface during printing process, positional shifts may occur after the extrusion of bioink due to insufficient temperature-sensitive crosslinking and the gravitational effects on the extruded filaments. In the future, upgrading the printing end-effector for simultaneous photo-crosslinking after extrusion[54] could enhance the crosslinking stability of the hydrogel, thereby mitigating the tendency for structural downward sliding observed in the current *in situ* bioprinting process.

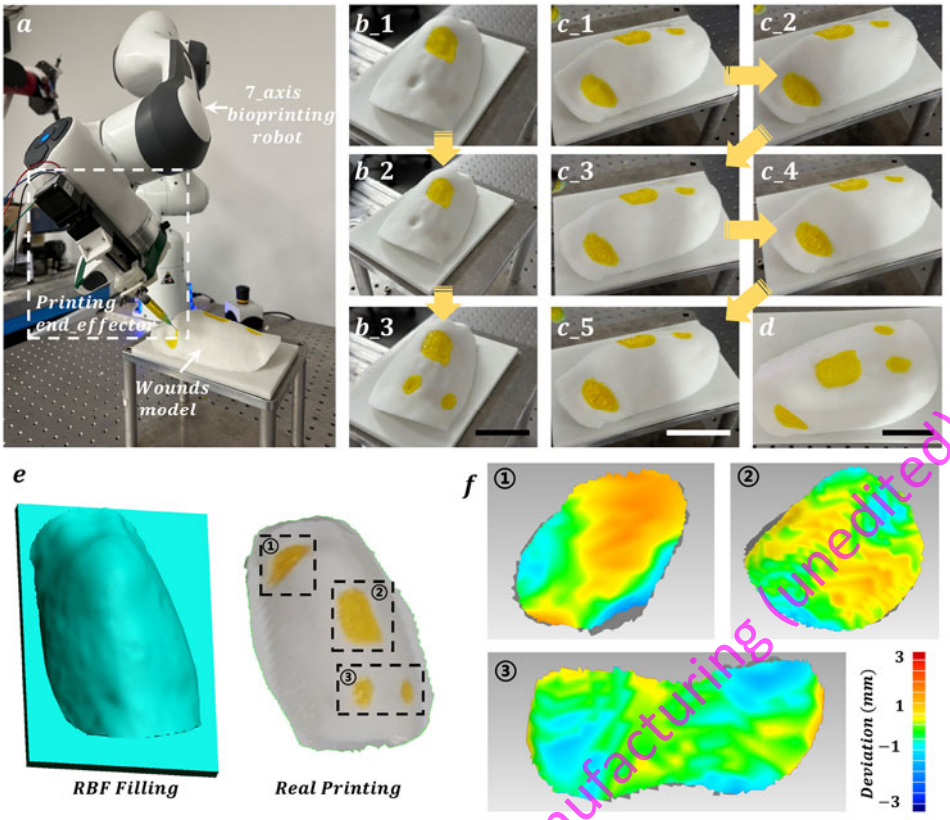

Figure 13. ***In situ*** **bioprinting demonstration on mouse back wound model.** **a,** Photo of the 7-axis bioprinting robot and the model. **b,** Process images of printing and repairing wounds 2-3 (Scale bar: 5 cm). **c,** Process images of printing and repairing wound 1 (the deepest wound, Scale bar: 5 cm). **d,** The bioprinting repaired back wound model (Scale bar: 5 cm). **e,** Comparison between the back model after RBF repair and the 3D scanned model after bioprinting repair. **f,** Comparative images of the differences on various wound. The average deviations for wounds 1-3 are 0.90 ± 0.74 mm, 0.52 ± 0.49 mm, 0.53 ± 0.70 mm, respectively, with a maximum deviation of 2.12 mm.

The quantitative evaluation of the printing results was conducted following the description in Section 2.7. (Fig. 13d). The dimensional discrepancies after repairing three wounds are statistically presented on the right, with average deviations of 0.90 ± 0.74 mm, 0.52 ± 0.49 mm, 0.53 ± 0.70 mm for wounds 1-3, respectively, and a maximum deviation of 2.12 mm (Fig. 13e). Setting aside the inherent errors of the 3D scanner and the deviations during the two model's registration, the constructed skin-like structure through *in situ* bioprinting essentially reproduces the appearance of undamaged skin. There are no significant boundaries observed between the wound edges and the printed structure, which indicates the high degree of conformity between the constructed structure and the shape of the wound. Quantitative analysis suggests the

feasibility of the conformal path planning algorithm and its guidance for *in situ* bioprinting, further highlighting the potential of this study in advancing 3D bioprinting for treating skin injuries.

4. Conclusion

In conclusion, the study introduces an effective conformal path planning algorithm based on optimization principles, demonstrating effective and accurate path generation for *in situ* bioprinting on complex and irregular surface. The algorithm, meticulously balancing shape and angle preservation, generates paths that faithfully replicate original planar designs, minimizing errors in both distance and angle. The systematic analysis of the step size parameter sheds light on the crucial trade-off between computation complexity and mapping error. Furthermore, comparative evaluations against direct-project paths highlight the algorithm's advantages in maintaining equidistance and angle fidelity, particularly significant in applications such as 3D bioprinting and antenna fabrication. And the final practical bioprinting experiments, including applications on diverse surfaces and complex skin wounds, validate the algorithm's efficacy. The *in situ* bioprinting process consistently present high fidelity in reproducing predetermined paths, ensuring minimal deviations and effective wound coverage.

This research contributes to the progression of *in situ* bioprinting technology, providing a systematic approach for precise path planning on irregular surfaces. The proposed algorithm opens avenues for customizable treatment of volumetric injuries, emphasizing its potential in advancing 3D bioprinting for various tissue types and injuries. Future work may involve refining the printing process, exploring additional optimization strategies, and extending applications to broader medical contexts.

Author contributions

Conceptualization: Wenxiang Zhao, Chuxiong Hu; Methodology: Wenxiang Zhao, Chuxiong Hu, Yunan Wang; Formal analysis and investigation: Wenxiang Zhao, Yunan Wang, Shize Lin; Writing - original draft preparation:Wenxaing Zhao; Writing - review and editing: all authors; Funding acquisition: Chuxiong Hu, Ze Wang; Resources: Chuxiong Hu; Supervision: Chuxiong Hu, Tao Xu.

Acknowledgments

This work was supported in part by National Key Research and Development Program of China under Grant 2023YFB4302003, and in part by National Natural Science Foundation of China under Grant 52205532.

Compliance with ethics guidelines

All authors declare no conflict of interest.

References

[1] Venus M, Waterman J and McNab I 2010 Basic physiology of the skin *Surgery (Oxford)* **28** 469-72

[2] Sun B K, Siprashvili Z and Khavari P A 2014 Advances in skin grafting and treatment of cutaneous wounds *Science* **346** 941-5

[3] Shpichka A, Butnaru D, Bezrukov E A, Sukhanov R B, Atala A, Burdukovskii V, Zhang Y and Timashev P 2019 Skin tissue regeneration for burn injury *Stem cell research & therapy* **10** 1-16

[4] Tarassoli S P, Jessop Z M, Al-Sabah A, Gao N, Whitaker S, Doak S and Whitaker I S 2018 Skin tissue engineering using 3D bioprinting: An evolving research field *Journal of Plastic, Reconstructive & Aesthetic Surgery* **71** 615-23

[5] Daikuara L Y, Chen X, Yue Z, Skropeta D, Wood F M, Fear M W and Wallace G G 2022 3D bioprinting constructs to facilitate skin regeneration *Advanced Functional Materials* **32** 2105080

[6] Weng T, Zhang W, Xia Y, Wu P, Yang M, Jin R, Xia S, Wang J, You C and Han C 2021 3D bioprinting for skin tissue engineering: Current status and perspectives *Journal of tissue engineering* **12** 20417314211028574

[7] He P, Zhao J, Zhang J, Li B, Gou Z, Gou M and Li X 2018 Bioprinting of skin constructs for wound healing *Burns & trauma* **6**

[8] Zhao W, Hu C and Xu T 2023 In vivo bioprinting: Broadening the therapeutic horizon for tissue injuries *Bioactive Materials* **25** 201-22

[9] Singh S, Choudhury D, Yu F, Mironov V and Naing M W 2020 In situ bioprinting–bioprinting from benchside to bedside? *Acta biomaterialia* **101** 14-25

[10] Albanna M, Binder K W, Murphy S V, Kim J, Qasem S A, Zhao W, Tan J, El-Amin I B, Dice D D and Marco J 2019 In situ bioprinting of autologous skin cells accelerates wound healing of extensive excisional full-thickness wounds *Scientific reports* **9** 1856

[11] Zhao W, Chen H, Zhang Y, Zhou D, Liang L, Liu B and Xu T 2022 Adaptive multi-degree-of-freedom in situ bioprinting robot for hair-follicle-inclusive skin repair: A preliminary study conducted in mice *Bioengineering & Translational Medicine* **7** e10303

[12] Di Bella C, Duchi S, O'Connell C D, Blanchard R, Augustine C, Yue Z, Thompson F, Richards C, Beirne S and Onofrillo C 2018 In situ handheld three-dimensional bioprinting for cartilage regeneration *Journal of tissue engineering and*

regenerative medicine **12** 611-21

[13] Moncal K K, Gudapati H, Godzik K P, Heo D N, Kang Y, Rizk E, Ravnic D J, Wee H, Pepley D F and Ozbolat V 2021 Intra-operative bioprinting of hard, soft, and hard/soft composite tissues for craniomaxillofacial reconstruction *Advanced functional materials* **31** 2010858

[14] Zhao W, Hu C, Xu T, Lin S, Wang Z and Zhu Y 2022 Subaqueous Bioprinting: A Novel Strategy for Fetal Membrane Repair with 7 - Axis Robot - Assisted Minimally Invasive Surgery *Advanced Functional Materials* **32** 2207496

[15] Russell C S, Mostafavi A, Quint J P, Panayi A C, Baldino K, Williams T J, Daubendiek J G, Hugo Sánchez V, Bonick Z and Trujillo-Miranda M 2020 In situ printing of adhesive hydrogel scaffolds for the treatment of skeletal muscle injuries *ACS Applied Bio Materials* **3** 1568-79

[16] Alkadi F, Lee K-C, Bashiri A H and Choi J-W 2020 Conformal additive manufacturing using a direct-print process *Additive Manufacturing* **32** 100975

[17] Chen L, Chung M-F, Tian Y, Joneja A and Tang K 2019 Variable-depth curved layer fused deposition modeling of thin-shells *Robotics and Computer-Integrated Manufacturing* **57** 422-34

[18] Nayyeri P, Zareinia K and Boughehara H 2022 Planar and nonplanar slicing algorithms for fused deposition modeling technology: A critical review *The International Journal of Advanced Manufacturing Technology* **119** 2785-810

[19] Wang H, Lian Q, Li D, Li C, Zhao T and Liang J 2021 Multi-tissue layering and path planning of in situ bioprinting for complex skin and soft tissue defects *Rapid Prototyping Journal* **27** 321-32

[20] Mitropoulou I, Bernhard M and Dillenburger B 2020 Print Paths Key-framing: Design for non-planar layered robotic FDM printing. In: *Proceedings of the 5th annual ACM symposium on computational fabrication,* pp 1-10

[21] Mitropoulou I, Bernhard M and Dillenburger B 2022 Nonplanar 3D printing of bifurcating forms *3D Printing and Additive Manufacturing* **9** 189-202

[22] Fortunato G M, Nicoletta M, Batoni E, Vozzi G and De Maria C 2023 A fully automatic non-planar slicing algorithm for the additive manufacturing of complex geometries *Additive Manufacturing* **69** 103541

[23] Yigit I E and Lazoglu I 2020 Spherical slicing method and its application on robotic additive manufacturing *Progress in Additive Manufacturing* **5** 387-94

[24] Yigit I E and Lazoglu I 2019 Helical slicing method for material extrusion-based

robotic additive manufacturing *Progress in Additive Manufacturing* **4** 225-32

[25] Yigit I E, Khan S A and Lazoglu I 2022 Robotic additive turning with a novel cylindrical slicing method *The International Journal of Advanced Manufacturing Technology* **119** 7641-51

[26] Zou Q and Zhao J 2013 Iso-parametric tool-path planning for point clouds *Computer-Aided Design* **45** 1459-68

[27] Fortunato G M, Rossi G, Bonatti A F, De Acutis A, Mendoza-Buenrostro C, Vozzi G and De Maria C 2021 Robotic platform and path planning algorithm for in situ bioprinting *Bioprinting* **22** e00139

[28] Fortunato G M, Batoni E, Bonatti A F, Vozzi G and De Maria C 2022 Surface reconstruction and tissue recognition for robotic-based in situ bioprinting *Bioprinting* **26** e00195

[29] Kucukdeger E, Tong Y, Singh M, Zhang J, Harding L K, Salado A, Ellingson S W and Johnson B N 2021 Conformal 3D printing of non-planar antennas on wrinkled and folded kapton films using point cloud data *Flexible and Printed Electronics* **6** 044002

[30] Lian Q, Li X, Li D, Gu H, Bian W and He X 2019 Path planning method based on discontinuous grid partition algorithm of point cloud for in situ printing *Rapid Prototyping Journal* **25** 602-13

[31] Zhou C, Yang Y, Wang J, Wu Q, Gu Z, Zhou Y, Liu X, Yang Y, Tang H and Ling Q 2021 Ferromagnetic soft catheter robots for minimally invasive bioprinting *Nature communications* **12** 5072

[32] Rodriguez-Padilla C, Cuan-Urquizo E, Roman-Flores A, Gordillo J L and Vázquez-Hurtado C 2021 Algorithm for the conformal 3D printing on non-planar tessellated surfaces: applicability in patterns and lattices *Applied Sciences* **11** 7509

[33] Huang Y, Wu H, Zhu C, Xiong W, Chen F, Xiao L, Liu J, Wang K, Li H and Ye D 2021 Programmable robotized 'transfer-and-jet'printing for large, 3D curved electronics on complex surfaces *International Journal of Extreme Manufacturing* **3** 045101

[34] Jafari B H and Gans N 2020 Surface parameterization and trajectory generation on regular surfaces with application in robot-guided deposition printing *IEEE Robotics and Automation Letters* **5** 6113-20

[35] Weingartshofer T, Haddadi A, Hartl-Nesic C and Kugi A 2022 Flexible Robotic Drawing on 3D Objects with an Industrial Robot. In: *2022 IEEE Conference on*

Control Technology and Applications (CCTA): IEEE) pp 29-36

[36] Bomze I M, Demyanov V F, Fletcher R, Terlaky T, Pólik I and Terlaky T 2010 Interior point methods for nonlinear optimization *Nonlinear Optimization: Lectures given at the CIME Summer School held in Cetraro, Italy, July 1-7, 2007* 215-76

[37] Korenius T, Laurikkala J and Juhola M 2007 On principal component analysis, cosine and Euclidean measures in information retrieval *Information Sciences* **177** 4893-905

[38] Qian G, Sural S, Gu Y and Pramanik S 2004 Similarity between Euclidean and cosine angle distance for nearest neighbor queries. In: *Proceedings of the 2004 ACM symposium on Applied computing,* pp 1232-7

[39] Zhao D and Guo W 2020 Shape and performance controlled advanced design for additive manufacturing: a review of slicing and path planning *Journal of Manufacturing Science and Engineering* **142** 010801

[40] Ozler S B, Bakirci E, Kucukgul C and Koc B 2017 Three-dimensional direct cell bioprinting for tissue engineering *Journal of Biomedical Materials Research Part B: Applied Biomaterials* **105** 2530-44

[41] Guo X, Xiao J and Wang Y 2018 A survey on algorithms of hole filling in 3D surface reconstruction *The Visual Computer* **34** 93-103

[42] Vedaldi A and Fulkerson B 2010 VLFeat: An open and portable library of computer vision algorithms. In: *Proceedings of the 18th ACM international conference on Multimedia,* pp 1469-72

[43] Zhao W, Hu C, Lin S, Wang Y, Liu L, Wang Z, Zhu Y and Xu T 2023 A closed-loop minimally invasive 3D printing strategy with robust trocar identification and adaptive alignment *Additive Manufacturing* **73** 103701

[44] Chen M H, Wang L L, Chung J J, Kim Y-H, Atluri P and Burdick J A 2017 Methods to assess shear-thinning hydrogels for application as injectable biomaterials *ACS biomaterials science & engineering* **3** 3146-60

[45] Olofsson B 2015 *Topics in machining with industrial robot manipulators and optimal motion control*: Department of Automatic Control, Lund University)

[46] Shembekar A V, Yoon Y J, Kanyuck A and Gupta S K 2019 Generating robot trajectories for conformal three-dimensional printing using nonplanar layers *Journal of Computing and Information Science in Engineering* **19** 031011

[47] Weiss V, Andor L, Renner G and Várady T 2002 Advanced surface fitting

techniques *Computer Aided Geometric Design* **19** 19-42

[48] Pratt V 1987 Direct least-squares fitting of algebraic surfaces *ACM SIGGRAPH computer graphics* **21** 145-52

[49] Wang J and Yu Z 2011 Quadratic curve and surface fitting via squared distance minimization *Computers & Graphics* **35** 1035-50

[50] Huang Y, Wu H, Xiao L, Duan Y, Zhu H, Bian J, Ye D and Yin Z 2019 Assembly and applications of 3D conformal electronics on curvilinear surfaces *Materials Horizons* **6** 642-83

[51] Adams J J, Duoss E B, Malkowski T F, Motala M J, Ahn B Y, Nuzzo R G, Bernhard J T and Lewis J A 2011 Conformal printing of electrically small antennas on three-dimensional surfaces *Advanced Materials* **23** 1335-40

[52] Ding H and Chang R C 2018 Simulating image-guided in situ bioprinting of a skin graft onto a phantom burn wound bed *Additive Manufacturing* **22** 708-19

[53] Fu Z, Naghieh S, Xu C, Wang C, Sun W and Chen X 2021 Printability in extrusion bioprinting *Biofabrication* **13** 033001

[54] Fortunato G M, Batoni E, Pasqua I, Nicoletta M, Vozzi G and De Maria C 2023 Automatic Photo-Cross-Linking System for Robotic-Based In Situ Bioprinting *ACS Biomaterials Science & Engineering* **9** 6926-34